



Cite this: *Nanoscale Horiz.*, 2023, 8, 794

Received 23rd December 2022,  
Accepted 14th March 2023

DOI: 10.1039/d2nh00591c

[rsc.li/nanoscale-horizons](https://rsc.li/nanoscale-horizons)

## An ultra-sensitive NH<sub>3</sub> gas sensor enabled by an ion-in-conjugated polycroconaine/Ti<sub>3</sub>C<sub>2</sub>T<sub>x</sub> core-shell composite†

Jin Zhou,<sup>a</sup> Seyed Hossein Hosseini Shokouh,<sup>a</sup> Linfan Cui,<sup>b</sup> Topias Järvinen,<sup>a</sup> Olli Pitkänen,<sup>a</sup> Zhong-Peng Lv<sup>b\*</sup> and Krisztian Kordas<sup>a\*</sup>

MXenes are emerging sensing materials due to their metallic conductivity and rich surface chemistry for analytes; they, however, suffer from poor stability. Incorporation with functional polymers can largely prevent the performance decay and enhance the sensing performance. Herein, we demonstrate a core-shell composite, Ti<sub>3</sub>C<sub>2</sub>T<sub>x</sub>@croconaine (poly(1,5-diaminonaphthalene-croconaine), PDAC) prepared by a facile *in situ* polymerization reaction, suitable for NH<sub>3</sub> detection. Compared to pristine Ti<sub>3</sub>C<sub>2</sub>T<sub>x</sub>, the sensor made of a Ti<sub>3</sub>C<sub>2</sub>T<sub>x</sub>-polycroconaine composite exhibits a significantly enhanced sensitivity of 2.8% ppm<sup>-1</sup> and an estimated achievable limit of detection of 50 ppb. The improved sensing performance could be attributed to the presence of PDAC facilitating the adsorption of NH<sub>3</sub> and changing the tunneling conductivity between Ti<sub>3</sub>C<sub>2</sub>T<sub>x</sub> domains. Density functional theory (DFT) calculations reveal that the adsorption energy of NH<sub>3</sub> on PDAC is the highest among the tested gases, which supports the selectivity of the sensor to this analyte. Benefiting from the protection conferred by the PDAC shell, the composite has a reliable operation period of at least 40 days. In addition, we demonstrated a flexible paper-based sensor of the Ti<sub>3</sub>C<sub>2</sub>T<sub>x</sub>@PDAC composite, without attenuated performance upon mechanical deformation. This work proposed a novel mechanism and a feasible methodology to synthesize MXene-polymer composites with improved sensitivity and stability for chemical sensing.

## 1. Introduction

Accidental ammonia (NH<sub>3</sub>) emissions and leakages from industrial operations and from difficult to control agricultural

### New concepts

2-dimensional metal carbides and nitrides (MXenes) are an emerging class of chemical sensing materials. The conventional strategies for enhancing the sensitivity were achieved by intercalation or forming porous structures. However, there is always a tradeoff between sensitivity and stability, where the larger MXene surface is more sensitive to oxidation. In this work, we demonstrate a new concept of using Ti<sub>3</sub>C<sub>2</sub>T<sub>x</sub> MXene@ ion-in-conjugated polymer core-shell structure to fabricate an NH<sub>3</sub> sensor which enables both ultrahigh sensitivity and significantly improved stability. The synthesis is done by a facile core assembly of Ti<sub>3</sub>C<sub>2</sub>T<sub>x</sub> flakes in the poor solvent, followed by *in situ* polymerization of the polymer shell. The ion-in-conjugate polymer shell served as a “sensitized layer” for gas adsorption and charge-transfer medium between analytes and the MXene core and protected the MXene core from oxidation. The electron tunneling among isolated domains further enhanced sensing sensitivity. Our new concept of using a core-shell structure has paved the way to solving the dilemma of sensitivity and stability for MXene-based gas sensors.

activities pose the potential risk of air pollution and contamination of waters with direct adverse effects on the biosphere, and also indirectly affect the society and economy.<sup>1–3</sup> Therefore, developing robust NH<sub>3</sub> sensors with high sensitivity is crucial. Among the different technologies, chemiresistive gas sensors offer cost-effective simple solutions for detecting ammonia.<sup>4,5</sup> The active sensing elements of such devices are typically based on inorganic semiconducting metal oxides that require elevated operation temperatures for sufficient electrical/ionic conductivity, stability, and efficient analyte desorption for sensor recovery.<sup>6,7</sup> To circumvent the intrinsic problems of metal oxide based sensors, contemporary research is drifting towards low-dimensional carbon nanomaterials,<sup>4,8</sup> layered transition metal dichalcogenides<sup>9–11</sup> and conductive polymers/composites,<sup>12,13</sup> whose chemistry and structure can be tuned to engineer their gas adsorption/desorption behavior, surface active site density, and electrical transport properties.

Recently, two-dimensional metal carbides and nitrides (MXenes) have been recognized as a new class of gas sensing

<sup>a</sup> Microelectronics Research Unit, Faculty of Information Technology and Electrical Engineering, University of Oulu, P.O. Box 4500, FIN-90014 Oulu, Finland.  
E-mail: [krisztian.kordas@oulu.fi](mailto:krisztian.kordas@oulu.fi)

<sup>b</sup> Department of Chemical and Metallurgical Engineering, Aalto University, FIN-00076 Aalto, Finland

<sup>c</sup> Department of Applied Physics, Aalto University, FIN-00076 Aalto, Finland.  
E-mail: [zhongpeng.lyu@aalto.fi](mailto:zhongpeng.lyu@aalto.fi)

† Electronic supplementary information (ESI) available. See DOI: <https://doi.org/10.1039/d2nh00591c>



materials,<sup>14–16</sup> owing to their good electrical conductivity, high signal-to-noise ratio,<sup>17</sup> rich surface chemistry with various terminal groups (–OH, –O and –F) and mechanical flexibility.<sup>18</sup> However, their easy oxidation under ambient conditions compromises long-term stability and sensitivity (0.06% ppm<sup>–1</sup> for NH<sub>3</sub> detection using Ti<sub>3</sub>C<sub>2</sub>T<sub>x</sub> reported by Wu *et al.*<sup>19</sup>), and challenges practical applications. To solve this issue, composites of Ti<sub>3</sub>C<sub>2</sub>T<sub>x</sub> with organic semiconductors provide promising alternatives owing to the formation of p–n or Schottky junctions in the composites among other synergistic effects,<sup>20–22</sup> where the structure of the organic semiconductors/conductor composites need to be carefully designed to maximize the sensing performance.

Ion-in-conjugated organic semiconductors, such as squaraines and croconaines, are emerging materials for chemiresistive gas sensors since their ionic moiety can interact with gas analytes through ion (or dipole)–dipole attraction and hydrogen bonds, leading to ultrahigh sensitivity.<sup>23,24</sup> However, their extremely low intrinsic conductivity and long response/recovery time make them difficult to fabricate practical devices.<sup>25</sup> Therefore, for gas sensing applications, ion-in-conjugated organic semiconductors and MXenes are expected to perfectly complement each other, in which the former ones have high sensitivity and stability, whereas the latter materials enhance the conductivity of the composite. Furthermore, due to their intense electron-delocalization, ion-in-conjugated organic semiconductors are also expected to interact with the negatively charged MXene surfaces to form a stable heterointerface.<sup>26</sup> Our previous study showed that polysquaraine (PDDS) intercalated Ti<sub>3</sub>C<sub>2</sub>T<sub>x</sub> has high sensitivity (2.2% ppm<sup>–1</sup>) for NH<sub>3</sub> detection,<sup>27</sup> with reasonably good stability. However, for practical applications, we need to further improve both the long-term stability and sensitivity, and thus new synthetic strategies are yet to be explored.

In this work, we have developed a assembly strategy in a poor solvent to fabricate core–shell composites of a Ti<sub>3</sub>C<sub>2</sub>T<sub>x</sub> MXene and ion-in-conjugated polymer, poly(1,5-diaminonaphthalene-croconaine) (PDAC), where well-delaminated Ti<sub>3</sub>C<sub>2</sub>T<sub>x</sub> was first assembled into particles in ethanol of low polarity, and then the PDAC was grafted outside the particles by an *in situ* polymerization synthesized of croconic acid and organic amines. The chemiresistive sensor of the obtained core–shell composite exhibited good selectivity, sensitivity, repeatability, low detection limit, and long-term stability over a period of at least 40 days, superior to the most reported MXene sensors so far.<sup>19–22,28</sup> Furthermore, we also show flexible sensor devices by simply brush coating the hybrid material on ordinary printing paper that can be folded/rolled without compromising its functionality. The good NH<sub>3</sub> sensing performance could be ascribed to the core–shell like geometry of Ti<sub>3</sub>C<sub>2</sub>T<sub>x</sub>@PDAC, in which the polymer shell prevents oxidation of the inorganic core, and the electron tunneling among the particles is highly sensitive to the gas adsorption on the shell. DFT calculations confirm that the PDAC facilitates the adsorption of NH<sub>3</sub>, with a binding energy of 0.72 eV, which is the highest among all tested gases. From our results, we demonstrate that the core–shell geometry with the combination of gas sensitive ion-in-conjugation

polymers with electrically conductive nanostructured fillers is a robust and plausible strategy to produce engineered sensing materials.

## 2. Results and discussion

### 2.1. Materials characterization

The preparation of Ti<sub>3</sub>C<sub>2</sub>T<sub>x</sub>@PDAC composite is illustrated in Fig. 1a. Firstly, aqueous dispersion of Ti<sub>3</sub>C<sub>2</sub>T<sub>x</sub> flakes (Ti<sub>3</sub>C<sub>2</sub>T<sub>x</sub>–H<sub>2</sub>O) was redispersed in ethanol (Ti<sub>3</sub>C<sub>2</sub>T<sub>x</sub>–EtOH), where the flakes were assembled into multilayer Ti<sub>3</sub>C<sub>2</sub>T<sub>x</sub> particles due to limited dispersity of Ti<sub>3</sub>C<sub>2</sub>T<sub>x</sub> in ethanol of low polarity. The ethanol suspension of Ti<sub>3</sub>C<sub>2</sub>T<sub>x</sub> particles was then mixed with croconic acid in ethanol, forming croconic acid coated Ti<sub>3</sub>C<sub>2</sub>T<sub>x</sub> particles (Ti<sub>3</sub>C<sub>2</sub>T<sub>x</sub>@croconic acid). The croconic acid shell on the particles was converted to PDAC by *in situ* polymerization with 1,5-diaminonaphthalene in a mixture of *n*-butanol/*o*-dichlorobenzene under the protection of N<sub>2</sub>, where the target Ti<sub>3</sub>C<sub>2</sub>T<sub>x</sub>@PDAC particles were obtained (see the Experimental section for details).<sup>29</sup> To optimize the sensing performance of the composite, three mass ratios of Ti<sub>3</sub>C<sub>2</sub>T<sub>x</sub>, croconic acid, and 1,5-diaminonaphthalene (15:3:3, 15:5:5, and 15:8:8) were surveyed and denoted as PM1, PM2, and PM3, respectively (Fig. S1, ESI<sup>†</sup>). To confirm that the PDAC was synthesized successfully in the presence of Ti<sub>3</sub>C<sub>2</sub>T<sub>x</sub> flakes, and that the two phases are interacting with each other (if they are interacting), we performed Fourier-transform infrared (FTIR) and Raman spectroscopy analyses. As shown in Fig. 1b, PM2 exhibits new peaks at 1586, 1545, 1511, 1408, 1365, 790, 695, and 580 cm<sup>–1</sup> originating from PDAC (in addition to the spectrum of pristine Ti<sub>3</sub>C<sub>2</sub>T<sub>x</sub>). Specifically, the peaks at 1586 and 1545 cm<sup>–1</sup> are the stretching vibrations of C=O in the croconyl moiety;<sup>30</sup> the peak at 1365 cm<sup>–1</sup> can be assigned to the –N=C– or –C=C– stretching;<sup>31</sup> and the peaks at 790, 695 and 580 cm<sup>–1</sup> are from the vibration of aromatic H.<sup>32</sup> Similar features can be found in PM1 and PM3 as well (Fig. S2a, ESI<sup>†</sup>), and the characteristic peaks of PDAC in the composites are more distinct as the content of PDAC in those is higher. Raman spectra of Ti<sub>3</sub>C<sub>2</sub>T<sub>x</sub>@PDAC composites exhibit two wide peaks at 1338 and 1565 cm<sup>–1</sup> which match the peaks in the PDAC spectrum (Fig. 1c and Fig. S2b, ESI<sup>†</sup>), indicating the amorphous structure of PDAC. Furthermore, the peaks at 124, 201, 582, and 722 cm<sup>–1</sup> correspond to the resonance peak, A<sub>1g</sub> (Ti, O, C), M–T<sub>x</sub>, and A<sub>1g</sub>(C) peaks in Ti<sub>3</sub>C<sub>2</sub>T<sub>x</sub>, respectively.<sup>33</sup> Peak-shifting (red dotted line) observed in both FTIR and Raman spectra indicates an interaction between PDAC and Ti<sub>3</sub>C<sub>2</sub>T<sub>x</sub>. In addition, a shift of ~2.55 eV of N 1s peak in the X-ray photoelectron spectrum (XPS) of PDAC in PM2 with reference to the pristine PDAC was observed (Fig. 1d) implying that the N species act as an electron donor in the interaction with Ti<sub>3</sub>C<sub>2</sub>T<sub>x</sub>.<sup>34</sup> Moreover, aromatic C and C–N peaks appeared in the C1s spectrum of PM2 further confirming the valid hybridization of PDAC and Ti<sub>3</sub>C<sub>2</sub>T<sub>x</sub> (Fig. S3, ESI<sup>†</sup>). Thermogravimetric analysis (TGA) of PDAC, Ti<sub>3</sub>C<sub>2</sub>T<sub>x</sub>, and composites was carried out by using synthetic air as the flowing gas (Fig. S4, ESI<sup>†</sup>). The mass ratio



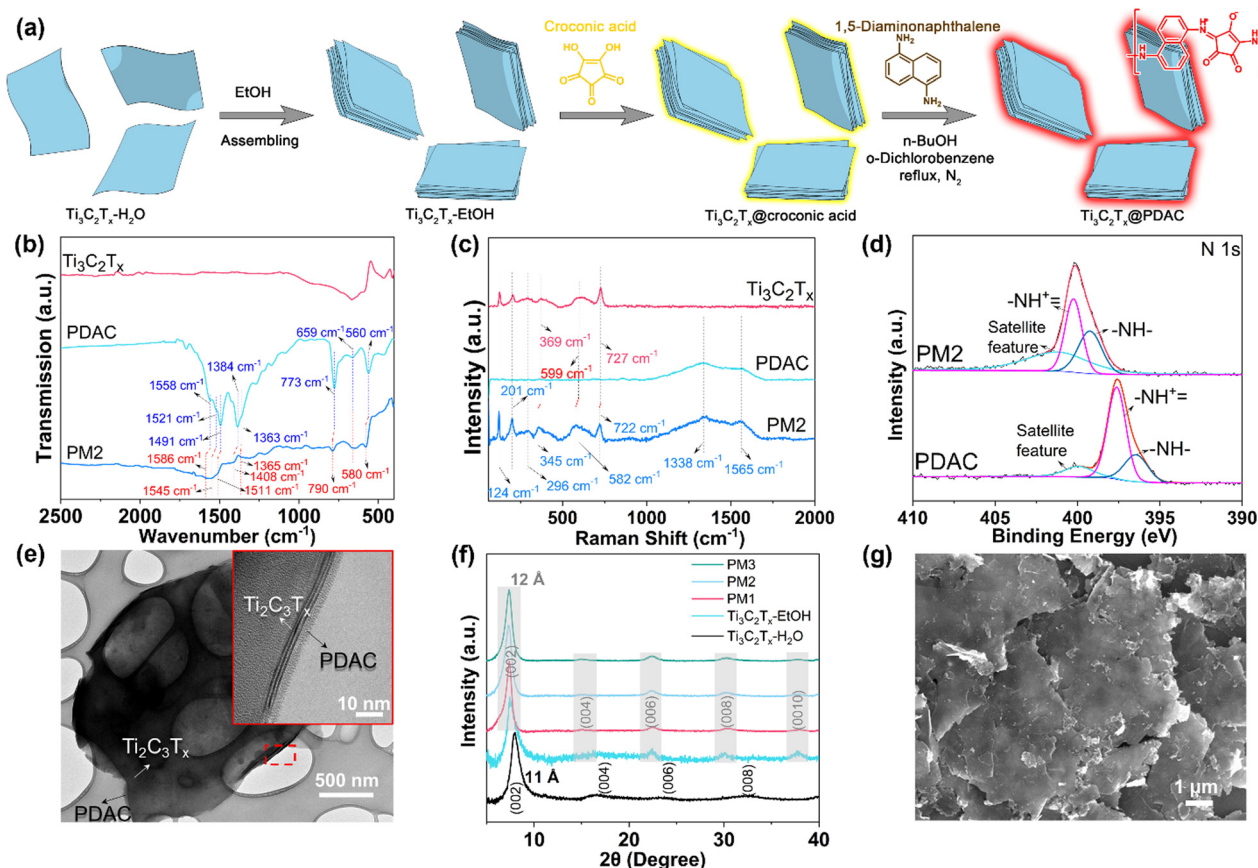


**Fig. 1** Synthesis, chemical, and structural characterization of  $\text{Ti}_3\text{C}_2\text{T}_x\text{@PDAC}$  composites. (a) Schematic illustration of preparation of  $\text{Ti}_3\text{C}_2\text{T}_x\text{@PDAC}$  structure. (b) FTIR and (c) Raman spectra of  $\text{Ti}_3\text{C}_2\text{T}_x$ , PDAC, and PM2. (d) X-ray photoelectron spectra of the N 1s region of PM2 and PDAC. (e) TEM image of PM2, inset HRTEM image. (f) XRD patterns (baseline subtracted) of the composites and pristine  $\text{Ti}_3\text{C}_2\text{T}_x$ . (g) SEM image of PM2.

of PDAC in the composites is calculated to be 17%, 25%, and 36% for PM1, PM2, and PM3, respectively.

The transmission electron microscopy (TEM) image of PM2 shows that the  $\text{Ti}_3\text{C}_2\text{T}_x$  flakes were covered by polymeric materials (Fig. 1e). High-resolution TEM (HRTEM) confirms the core-shell structure of  $\text{Ti}_3\text{C}_2\text{T}_x\text{@PDAC}$  (inset of Fig. 1e) where the amorphous PDAC shell is wrapped around the  $\text{Ti}_3\text{C}_2\text{T}_x$  core. The X-ray diffraction (XRD) patterns of PM1–3 and  $\text{Ti}_3\text{C}_2\text{T}_x\text{-EtOH}$  both show high order lamellar peaks, *e.g.* (0010), indicating a long-range assembly of the flakes induced by ethanol (Fig. 1f). We also find no diffraction peak shift among PM1–3 and  $\text{Ti}_3\text{C}_2\text{T}_x\text{-EtOH}$ , indicating no intercalation of PDAC during or after the polymerization. The slightly shifted (002) peak of the  $\text{Ti}_3\text{C}_2\text{T}_x\text{-EtOH}$  and the composites compared to  $\text{Ti}_3\text{C}_2\text{T}_x\text{-H}_2\text{O}$  indicates a 1 Å increase of the d-spacing, caused by the intercalant exchange from  $\text{H}_2\text{O}$  to an organic solvent used for synthesis.<sup>35</sup> The domain size in the out-of-plane direction can be estimated from the full width at half maximum of (002) peaks using the Scherrer equation. We found that the domain size increased slightly from 9.5 nm in pristine  $\text{Ti}_3\text{C}_2\text{T}_x$  to 10.3–11.5 nm in the composites. Scanning electron microscopy (SEM) revealed that  $\text{Ti}_3\text{C}_2\text{T}_x\text{@PDAC}$  composites have larger flakes with distinctive and straight edges (Fig. 1g and Fig. S5, ESI<sup>†</sup>), compared to pristine  $\text{Ti}_3\text{C}_2\text{T}_x$

(Fig. S5c, ESI<sup>†</sup>). Furthermore, energy-dispersive X-ray (EDX) mapping analysis of the composite PM2 revealed the homogeneous distribution of N element originating from PDAC (Fig. S6, ESI<sup>†</sup>). The structural characterizations confirm that the  $\text{Ti}_3\text{C}_2\text{T}_x\text{@PDAC}$  composite has a core-shell like structure where the well-assembled multilayer MXene cores were coated by the PDAC shell as indicated in Fig. 1a. It is interesting to note here that ethanol, as the poor solvent of  $\text{Ti}_3\text{C}_2\text{T}_x$  colloids, plays an important role in the formation of core-shell composites. In contrast, an intercalated polymer- $\text{Ti}_3\text{C}_2\text{T}_x$  structure was obtained in our previous work,<sup>27</sup> in which water, as a good solvent, was used for all the syntheses.

## 2.2. $\text{NH}_3$ sensing performance

To estimate the sensing performances of the composites, we deposited the PM1, PM2, and PM3 composites on chips ( $\text{Al}_2\text{O}_3$  substrate with 5 pairs of Ag-Pd interdigital electrodes) by drop-casting. The resistance of the sensors was logged using an Agilent 3458A multimeter, while introducing the analytes into the chamber at concentrations varying from 500 ppb to 10 ppm. The base resistance of the sensor devices significantly increases as the concentration of PDAC in the composites increases (Fig. S7, ESI<sup>†</sup>), and the fact that  $\text{NH}_3$  increases the resistance of the sensor devices suggests a p-type semiconductor-like



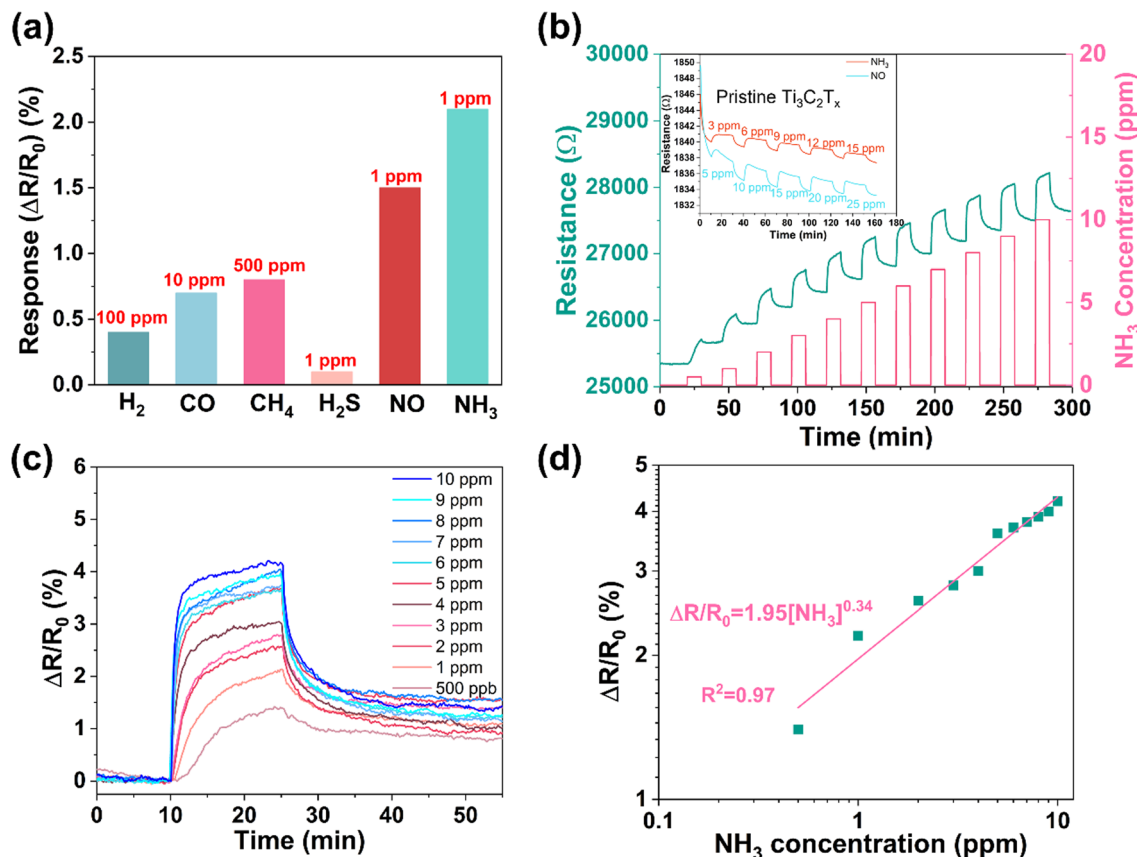


Fig. 2 Gas sensing of PM2 towards different analytes. (a) The selectivity of the sensor; (b) the real-time resistance of the sensor versus time curve, inset, the sensing performance of pristine  $\text{Ti}_3\text{C}_2\text{T}_x$ ; (c) response of the sensor measured for individual  $\text{NH}_3$  pulses; (d) double log plot and power function fit of data shown in panel (c).

behavior of the  $\text{Ti}_3\text{C}_2\text{T}_x$ @PDAC composite.<sup>36</sup> Back-gated field-effect transistor measurements that show increased channel current at negative gate bias further confirm the p-type behavior of the composite (Fig. S8, ESI†). Among the three sensors, the response of the PM2-based device is the highest and thus was selected for subsequent measurements (Fig. S7b, ESI†).

The selectivity of the sensor to various analytes (including  $\text{H}_2$ , CO,  $\text{CH}_4$ , and  $\text{H}_2\text{S}$  beside  $\text{NH}_3$ ) was assessed at room temperature (Fig. 2a and Fig. S9, ESI†). Each analyte was found to induce a positive change of resistance, regardless of its oxidizing or reducing nature. Similar behavior was reported for  $\text{Ti}_3\text{C}_2\text{T}_x$  in the pioneering study of Kim *et al.*<sup>37</sup> We also tested the effect of potentially interfering gases (CO, NO, and  $\text{H}_2\text{S}$  that induced pronouncedly higher sensitivity than  $\text{H}_2$  and  $\text{CH}_4$  in the original single analyte tests) on the sensory response to  $\text{NH}_3$ . The results measured for two-component mixtures show that the sensory response to the coexisting  $\text{H}_2\text{S}$ , CO, or NO in  $\text{NH}_3$  is a superposition of the responses; however, the change of the original output signal stemming from  $\text{NH}_3$  is not high (Fig. S10, ESI†). Among the applied analytes,  $\text{NH}_3$  induces the highest sensory response. To survey the sensing performance in more detail, we varied the concentration of  $\text{NH}_3$  in the range between 500 ppb and 10 ppm. Although the real-time resistance curves show increased response with the concentration (Fig. 2b), the

relationship is visibly not linear, and the baseline displays a drift (Note: in practice, the baseline drift may be calibrated by signal processing techniques, *e.g.*, multivariate regression algorithms or machine learning.<sup>38</sup>). To evaluate the sensor response more precisely, in a series of repeated measurements, we reduced the drift (and improved the sensor recovery) by applying longer (120 min) purging periods than those shown in Fig. 2b (15 min) and eliminated the variation of  $R_0$  by plotting  $\Delta R/R_0$  (Fig. 2c), in which  $R_0$  refers to the actual resistance measured at the moment of starting the gas pulse. The data indeed confirm that the sensor response is not linear, instead, it follows the power law with an exponent of 0.34 according to the fitting shown in Fig. 2c. Such behavior may be explained *via* the Langmuir adsorption model similar to those observed for other sensors.<sup>39,40</sup> Accordingly, the calculated highest sensitivity appears at the lowest applied analyte concentration (*i.e.* at 500 ppb  $\text{NH}_3$ ) having a value of 2.8%/ppm, which is significantly better than those published for pristine  $\text{Ti}_3\text{C}_2\text{T}_x$  (inset of Fig. 2b).<sup>37</sup> The corresponding theoretically achievable LOD for  $\text{NH}_3$  with the PM2 composite is only 50 ppb (according to the calculation shown in Fig. S11, ESI†).<sup>24</sup> It is worth noting that NO can also cause a significant response at low concentrations. Similar to that measured for  $\text{NH}_3$ , the sensor shows a nonlinear response and good repeatability for NO (Fig. S12, ESI†).





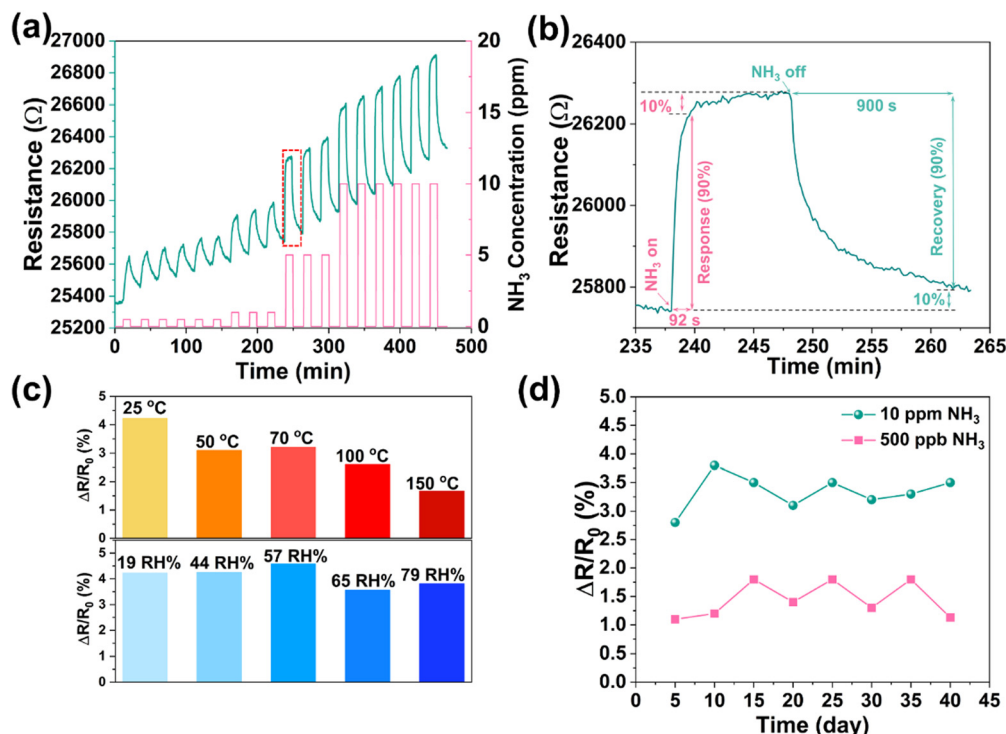


Fig. 3 Performance assessment and long-term stability of the PM2-based sensor. (a) Repeatability, (b) response/recovery time of PM2-based sensor; (c) temperature (top) and humidity effect (bottom) on the sensing performance of the sensor at 10 ppm NH<sub>3</sub>; and (d) sensing stability test in the period of 40 days.

The repeatability of the sensor (Fig. 3a) shows an acceptable variation in sequential NH<sub>3</sub> pulses, which are  $(0.9 \pm 0.1)\%$ ,  $(1.1 \pm 0.06)\%$ ,  $(2.1 \pm 0.02)\%$ , and  $(2.6 \pm 0.02)\%$  at 0.5, 1, 5 and 10 ppm, respectively. The response ( $t_{90\%}$ ) and recovery time ( $t_{10\%}$ ) of the sensor is about 1.5 min and 15.0 min, respectively (Fig. 3b). The temperature dependence of sensing performance investigated between 25 and 150 °C shows a decreased response with increased working temperature (Fig. 3c), which might be attributed to the oxidation of Ti<sub>3</sub>C<sub>2</sub>T<sub>x</sub> as well as the smaller adsorption constant at higher temperature.<sup>41</sup> The effect of humidity on the sensing performance is negligible in a relatively large range of humidity (from 19 RH% to 79 RH%), indicating a limited interaction of water with the surface (Fig. 3c). In addition, to evaluate the long-term stability of the sensor, we performed measurements for a period of 40 days (Fig. 3d and Fig. S13, ESI†) and found stable responses to individual NH<sub>3</sub> pulses *i.e.*  $(1.4 \pm 0.3)\%$  at 500 ppb and  $(3.3 \pm 0.3)\%$  at 10 ppm. Compared to the pristine Ti<sub>3</sub>C<sub>2</sub>T<sub>x</sub>, the improved stability of the composite may be caused by the coverage of the Ti<sub>3</sub>C<sub>2</sub>T<sub>x</sub> surface especially the defects with PDAC, hence protecting it from rapid oxidation.<sup>42</sup>

### 2.3. Fabrication of flexible sensors on paper

Fabrication of flexible sensors on biodegradable substrates is an important pathway for achieving sustainable electronics.<sup>43,44</sup> Inspired by the good mechanical adhesion of MXenes on cellulose/paper,<sup>45</sup> we fabricated a paper-based gas sensor using the PM2 composite by simply manually drawing patterns of the suspended composite (Fig. 4a). For the electrodes, four pairs of

interdigital fingers (line width and spacing of  $\sim 0.5$  mm) were hand-drawn on a paper sheet using a pencil of HB hardness (Fig. S14, ESI†), upon which a sensing layer of the PM2 composite was then brush coated. The resistance of the paper-based sensor was relatively stable (2.1% and 2.4% increase in a folded and rolled sensor, respectively) in different situations without gas flow (Fig. S15, ESI†). The NH<sub>3</sub> sensing performance of the paper-based sensor was surveyed in three different situations. As shown in Fig. 4b–d, the sensor shows a distinct response to NH<sub>3</sub> exposure and good recovery under air purging regardless of being kept flat, folded, or rolled. In addition, a spray-coated pattern is also performed (using a shadow stencil to obtain the pattern), indicating the feasibility of more sophisticated deposition techniques (Fig. S16, ESI†). These results suggest the feasibility of using our core-shell composites for a printed flexible sensor; in particular, it is expected to be applied in situations that require degradable electronic devices.

## 3. Mechanism

To understand the transport properties of Ti<sub>3</sub>C<sub>2</sub>T<sub>x</sub>@PDAC and pristine Ti<sub>3</sub>C<sub>2</sub>T<sub>x</sub>, we have measured their temperature-dependent resistance curves. The resistance ( $R$ ) of pristine Ti<sub>3</sub>C<sub>2</sub>T<sub>x</sub> increased with temperature proving its metallic conductivity, whereas the resistance of Ti<sub>3</sub>C<sub>2</sub>T<sub>x</sub>@PDAC shows the opposite trend, indicating the semiconductive nature of Ti<sub>3</sub>C<sub>2</sub>T<sub>x</sub>@PDAC (Fig. 5a and b). The temperature ( $T$ ) dependent electrical conductivity ( $\sigma \propto R^{-1}$ ) of most composites can be described by variable range hopping  $\sigma T^{0.5} = \exp(-BT^{-0.25})$  and/or tunnelling  $\sigma = \sigma_0 \exp(-AT^{-0.5})$  mechanism,<sup>46,47</sup>



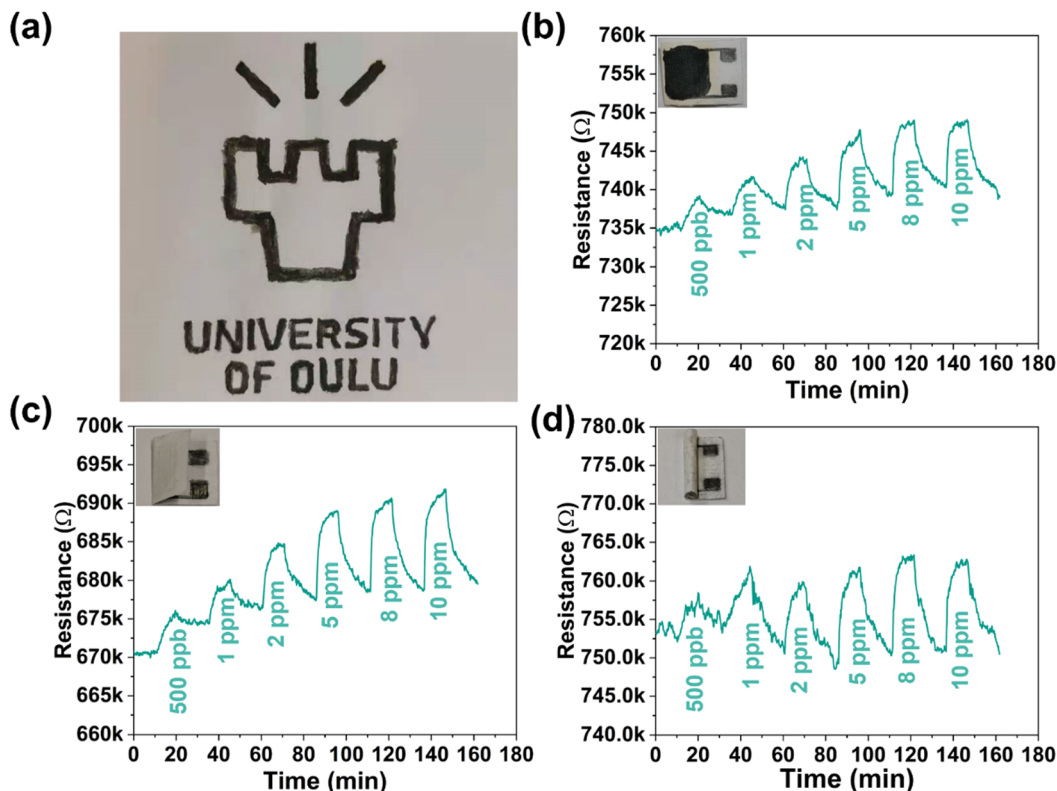


Fig. 4 Flexible sensor of PM2 on a paper-based substrate. (a) Logo of the University on a printing paper written in PM2 ink.  $\text{NH}_3$  sensing with devices hand-written on paper: (b) flat, (c) folded and (d) rolled.

where  $\sigma_0$ ,  $A$ , and  $B$  are constants. As shown in Fig. S17 (ESI<sup>†</sup>), for  $T > 240$  K, the plot of  $\ln(R^{-1})$  versus  $T^{-0.5}$  and  $\ln(R^{-1}T^{0.5})$  versus  $T^{-0.25}$  both show good linearity, which suggests that the electron transport between isolated  $\text{Ti}_3\text{C}_2\text{T}_x$  domains in PM2 is dominated by either hopping, tunneling, or a hybrid mechanism of both.<sup>48</sup> The interaction and charge transfer between the analytes and  $\text{Ti}_3\text{C}_2\text{T}_x$ @PDAC composites will change the tunneling/hopping conductivity. In the case of core-shell structures, the main active sites for the gas analytes are on the PDAC shell instead of  $\text{Ti}_3\text{C}_2\text{T}_x$  surface (Fig. 5c). DFT calculations prove that PDAC can provide active sites for various analytes including  $\text{NH}_3$ , NO, CO, etc. (with the adsorption modes shown in Fig. S18, ESI<sup>†</sup>). The simulation results (Table S1, ESI<sup>†</sup>) indicate that  $\text{NH}_3$  as an electron donor, compared to other tested analytes, induced the highest charge transfer ( $0.072 e$ ) and the highest adsorption energy ( $0.54$  eV). However, due to the strong interaction between the  $\text{Ti}_3\text{C}_2\text{T}_x$  and PDAC (Fig. 1d), the charge will further transfer from the PDAC shell to the  $\text{Ti}_3\text{C}_2\text{T}_x$  core and decrease the conductivity of  $\text{Ti}_3\text{C}_2\text{T}_x$ ,<sup>49</sup> and eventually decrease the tunneling/hopping conductivity among discrete domains in the composite.<sup>48</sup> The ultrahigh sensitivity can be attributed to two factors: (1) the PDAC shell here works as a “sensitized layer” that facilitates the gas adsorption and charge transport between the  $\text{Ti}_3\text{C}_2\text{T}_x$  core and gas analytes; (2) the core-shell geometry in the composite enables a tunneling transport mechanism, which is highly sensitive to the energy barrier within the tunneling junction. In contrast, in the controlled experiments, pristine  $\text{Ti}_3\text{C}_2\text{T}_x$  displays an inferior response (Fig. 2b), further

indicating that the presence of PDAC improves the sensing performance of the composite.

## 4. Conclusions

In conclusion, a  $\text{Ti}_3\text{C}_2\text{T}_x$ @PDAC composite with a core-shell structure is prepared *via* a facile *in situ* polymerization reaction of 1,5-diaminonaphthalene and croconic acid in the presence of  $\text{Ti}_3\text{C}_2\text{T}_x$ , where the  $\text{Ti}_3\text{C}_2\text{T}_x$  core is formed through assembly in a poor solvent. The  $\text{Ti}_3\text{C}_2\text{T}_x$ @PDAC composite exhibited good sensitivity ( $2.8\%$  ppm<sup>-1</sup>), selectivity, repeatability, and relatively fast response/recovery (186/552 s) for  $\text{NH}_3$  detection. The theoretical achievable limit of detection for our sensor is estimated to be 50 ppb  $\text{NH}_3$ . In particular, compared to pristine  $\text{Ti}_3\text{C}_2\text{T}_x$ , the long-term stability of the  $\text{Ti}_3\text{C}_2\text{T}_x$ @PDAC composite is significantly improved. The sensing performance can be ascribed to the presence of PDAC shell facilitating the interaction between composite and gas analytes, as well as the tunneling transport mechanism between the  $\text{Ti}_3\text{C}_2\text{T}_x$  domains. DFT calculations revealed that PDAC can form H-bonding with  $\text{NH}_3$  and induce the highest adsorption energy and value of the charge transfer among tested gases. Furthermore, we have demonstrated the ease of fabrication of a hand-drawn flexible sensor on ordinary paper with the composites, offering an environmentally friendly, simple, and affordable solution for disposable sensing devices.



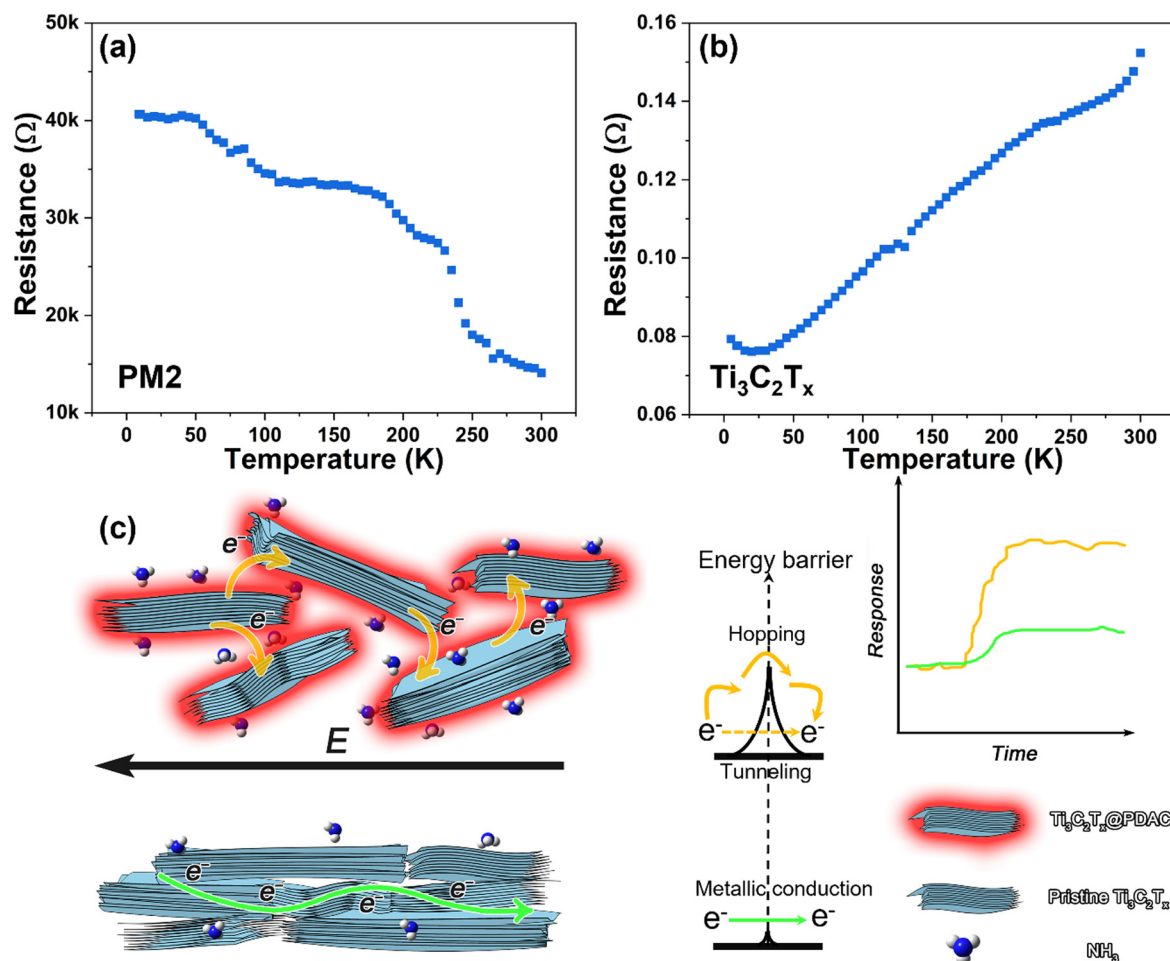


Fig. 5 Transport study and gas sensing mechanism of the  $\text{Ti}_3\text{C}_2\text{T}_x\text{@PDAC}$  composite. Temperature dependence of resistance change in (a) PM2 and (b) pristine  $\text{Ti}_3\text{C}_2\text{T}_x$ . (c) The suggested sensing mechanism of  $\text{Ti}_3\text{C}_2\text{T}_x\text{@PDAC}$  and pristine  $\text{Ti}_3\text{C}_2\text{T}_x$ .

## 5. Experimental section

### Synthesis of $\text{Ti}_3\text{C}_2\text{T}_x$

An aqueous dispersion of  $\text{Ti}_3\text{C}_2\text{T}_x$  was synthesized using the MILD method with minor modification.<sup>50</sup> In a typical recipe, 2 g  $\text{Ti}_3\text{AlC}_2$  (325 mesh, Carbon-Ukraine) was gradually added to a mixture of 40 mL 9 M HCl and 2 g LiF at 35 °C. After stirring for 24 h, the product was centrifuged and washed with deionized water until pH > 5. Then, 40 mL of water was added to the sediment and vortex for 30 min. The mixture was centrifuged at 3500 rpm for 15 min to obtain the supernatant containing few and multiple layered  $\text{Ti}_3\text{C}_2\text{T}_x$  and then stored at 4 °C. To measure the  $\text{Ti}_3\text{C}_2\text{T}_x$  concentration, a certain volume of the  $\text{Ti}_3\text{C}_2\text{T}_x$  dispersion was vacuum dried and then the formed self-standing film was weighed.

### $\text{Ti}_3\text{C}_2\text{T}_x\text{/PDAC}$ composite preparation

To prepare the  $\text{Ti}_3\text{C}_2\text{T}_x\text{@PDAC}$  composites, 30 mL ethanol suspension of  $\text{Ti}_3\text{C}_2\text{T}_x$  ( $0.5 \text{ mg mL}^{-1}$ ) was initially prepared, by redispersing 930  $\mu\text{L}$  of aqueous dispersion ( $16.2 \text{ mg mL}^{-1}$ ) of  $\text{Ti}_3\text{C}_2\text{T}_x$  in ethanol and stirred with croconic acid for 6 hours under  $\text{N}_2$  protection. Then, the mixture of  $\text{Ti}_3\text{C}_2\text{T}_x$  and croconic acid was dried at room

temperature and transferred to a 30 mL mixed solution of *n*-butanol and orthodichlorobenzene (1:1 in volume) with 1,5-diaminonaphthalene. The solution was bubbled by  $\text{N}_2$  for 20 min, and then stirred and refluxed for 13 hours under  $\text{N}_2$  protection. Finally, the  $\text{Ti}_3\text{C}_2\text{T}_x\text{@PDAC}$  composite was centrifuged and washed with acetone, ethanol, and deionized water; after washing, the composite was dispersed in ethanol (around  $12 \text{ mg mL}^{-1}$ ) for the following measurements. A composite with three mass ratios of  $\text{Ti}_3\text{C}_2\text{T}_x$ , croconic acid, and 1,5-diaminonaphthalene 15:3:3, 15:5:5, and 15:8:8 was synthesized (noted as PM1, PM2, and PM3, respectively).

PDAC was synthesized by dissolving 50 mg croconic acid and 50 mg 1,5-diaminonaphthalene into a 35 mL mixed solution of *n*-butanol and dichlorobenzene and reacting for 13 hours. The product, a dark powder, was collected by centrifuging and drying. The FTIR spectra of the reactants and PDAC are shown in Fig. S19 (ESI<sup>†</sup>).

### Characterization

X-ray photoelectron spectroscopy (XPS) measurements were performed with a Kratos Axis Ultra ESCA system with an Al K $\alpha$  source. The Raman spectra were obtained using a Thermo



Scientific DXR2xi Raman imaging microscope (excitation wavelength,  $\lambda = 785$  nm). The microstructure of the synthesized material was studied by field-emission scanning electron microscopy (FESEM, Zeiss ULTRA plus and equipped with EDX) and transmission electron microscopy (TEM, JEOL JEM-2200FS EFTEM/STEM 200 kV). Fourier transform infrared spectroscopy (FTIR) was performed on a Spectrum Two FT-IR spectrometer using an ATR model (PerkinElmer, UK). The X-ray diffraction (XRD) was performed using a Rigaku Smart Lab 9 kW, Cu K $\alpha$ -radiation. The thermal gravimetric analysis (TGA, Setaram Labsys) was carried out under a carrier gas of air with a rate of 10 °C min<sup>-1</sup> from room temperature to 800 °C. Temperature-dependent resistance was measured on a Quantum Design PPMS DynaCool Physical Property Measurement System (PPMS) in the constant current mode at 50  $\mu$ A.

### Fabrication of the sensor devices

Ethanol dispersion solution of the composite was drop-coated onto an Al<sub>2</sub>O<sub>3</sub> substrate which was printed with five pairs of Ag-Pd interdigitated electrodes (interdigital electrodes, the electrode distance and width are both 200  $\mu$ m) (14 mm  $\times$  7 mm, 0.64 mm in thickness) and dried at room temperature. The back-gate field-effect transistor device was fabricated by drop-coating the composite onto a highly doped Si/SiO<sub>2</sub> substrate with gold electrodes (drain and source), and the gate voltage was applied to the Si layer. The paper-based sensor was prepared by brushing the composite on the paper with 4 pairs of graphite interdigital electrodes. The graphite interdigital electrodes on the paper substrate were hand-drawn using a HB pencil, and each graphite electrode was dipped three times to ensure connection.

### Gas sensing test

The resistance of sensors was recorded in a Linkam THMS600 heating and freezing stage connected to an Agilent 3458A multimeter at 5 V of constant bias. The concentrations of NH<sub>3</sub>, NO, H<sub>2</sub>S, CH<sub>4</sub>, CO, and H<sub>2</sub> were diluted to the desired value by commercial synthetic air through mass flowmeters. The working temperature in measurements was set at room temperature (25 °C). To exclude the effect of flow rate on sensor resistance, the total gas flow rate was kept constant at 500 mL min<sup>-1</sup>. The sensing response is calculated as  $(R_g - R_0)/R_0$ , where  $R_0$  and  $R_g$  are the resistance values before and upon sensor device exposure to gas analytes. The sensor device based on pristine Ti<sub>3</sub>C<sub>2</sub>T<sub>x</sub> is made by drop-casting the supernatant of aqueous Ti<sub>3</sub>C<sub>2</sub>T<sub>x</sub> solution on the substrate. To obtain the NH<sub>3</sub> gas with different humidity, an additional air flow was bubbled into flasks containing water. The humidity was controlled by varying the gas flow rate and the wet gas was then mixed with the NH<sub>3</sub> gas. The final humidity of the test gas was calibrated using a commercial humidity sensor.

### DFT simulation

All theory calculations were conducted based on GGA-BLYP/DNP implemented in DMol3 code. Intermolecular weak interactions were semi-empirically corrected using the

Tkatchenko-Scheffler scheme.<sup>51</sup> The adsorption modes between PDAC and analytes were optimized until convergence within a standard of  $1 \times 10^{-5}$  Ha in energy and 0.002 Ha Å<sup>-1</sup> in residue force. Mulliken population analysis was applied to analyze charge transfer between PDAC and analytes. To simplify calculations, the repeat unit of PDAC is used for the simulations. Binding energy is defined as  $E = (E_{\text{PDAC}} + E_{\text{Gas}}) - E_{\text{PDAC+Gas}}$ , where  $E_{\text{PDAC}}$ ,  $E_{\text{gas}}$ ,  $E_{\text{PDAC+Gas}}$  represents the energy of the PDAC, the energy of gas molecules, and the total energy of the PDAC with the adsorbed gas molecule, respectively.

## Author contributions

J. Z. conducted the XRD, TGA, SEM, and electrical and sensor measurements and DFT calculations. Data analyses/plotting were performed by J. Z. and S. H. H. S. Raman, FTIR and PPMS measurements were performed by Z.-P. L. The synthesis of pristine MXene ink was done by L. C. and Z.-P. L. The shadow stencil for spray-coating was fabricated by T. J., O. P. and J. Z. The manuscript was drafted by J. Z. and then was discussed and revised by all co-authors.

## Conflicts of interest

There are no conflicts to declare.

## Acknowledgements

This work was financially supported in part by Walter Ahlström säätiö and China Scholarship Council. We acknowledge funding from the Academy of Finland (Center of Excellence Program in Life-inspired Hybrid Materials (LIBER, No. 346108) and Project No. 330214). The authors thank Dr Rhodri Mansell and Sreeveni Das for the assistance in materials synthesis and measurements, and the personnel of the Centre for Material Analysis at the University of Oulu for technical assistance. Prof. Hannu-Pekka Komsa (University of Oulu) is also greatly acknowledged for his comments on the manuscript.

## References

- 1 M. Van Damme, L. Clarisse, S. Whitburn, J. Hadji-Lazaro, D. Hurtmans, C. Clerbaux and P.-F. Coheur, *Nature*, 2018, **564**, 99–103.
- 2 Q. Wang, H. Fu, J. Ding, C. Yang and S. Wang, *Opt. Laser Technol.*, 2020, **125**, 106036.
- 3 S. Singh, J. Deb, U. Sarkar and S. Sharma, *ACS Appl. Nano Mater.*, 2020, **3**, 9375–9384.
- 4 C. Mackin, V. Schroeder, A. Zurutuza, C. Su, J. Kong, T. M. Swager and T. Palacios, *ACS Appl. Mater. Interfaces*, 2018, **10**, 16169–16176.
- 5 J. Wagner, H.-J. Jang, J. Han and H. E. Katz, *Mater. Horiz.*, 2020, **7**, 1358–1371.
- 6 S. Singh, J. Deb, U. Sarkar and S. Sharma, *ACS Sustainable Chem. Eng.*, 2021, **9**, 7328–7340.





- 7 A. G. Bannov, M. V. Popov, A. E. Brester and P. B. Kurmashov, *Micromachines*, 2021, **12**, 186.
- 8 L. A. Panes-Ruiz, M. Shaygan, Y. Fu, Y. Liu, V. Khavrus, S. Ostwald, T. Gemming, L. Baraban, V. Bezugly and G. Cuniberti, *ACS Sens.*, 2018, **3**, 79–86.
- 9 S. Singh, J. Deb, U. Sarkar and S. Sharma, *ACS Appl. Nano Mater.*, 2021, **4**, 2594–2605.
- 10 Y. Kim, S. Lee, J. Song, K. Y. Ko, W. J. Woo, S. W. Lee, M. Park, H. Lee, Z. Lee and H. Choi, *Adv. Funct. Mater.*, 2020, **30**, 2003360.
- 11 F. Urban, F. Giubileo, A. Grillo, L. Iemmo, G. Luongo, M. Passacantando, T. Foller, L. Madauß, E. Pollmann and M. P. Geller, *2D Mater.*, 2019, **6**, 45049.
- 12 S. Sharma, S. Hussain, S. Singh and S. S. Islam, *Sens. Actuators, B*, 2014, **194**, 213–219.
- 13 N. R. Tanguy, M. Thompson and N. Yan, *Sens. Actuators, B*, 2018, **257**, 1044–1064.
- 14 W. Yuan, K. Yang, H. Peng, F. Li and F. Yin, *J. Mater. Chem. A*, 2018, **6**, 18116–18124.
- 15 H.-Y. Li, C.-S. Lee, D. H. Kim and J.-H. Lee, *ACS Appl. Mater. Interfaces*, 2018, **10**, 27858–27867.
- 16 J. Choi, Y. Kim, S. Cho, K. Park, H. Kang, S. J. Kim and H. Jung, *Adv. Funct. Mater.*, 2020, **30**, 2003998.
- 17 S. J. Kim, H. J. Koh, C. E. Ren, O. Kwon, K. Maleski, S. Y. Cho, B. Anasori, C. K. Kim, Y. K. Choi, J. Kim, Y. Gogotsi and H. T. Jung, *ACS Nano*, 2018, **12**, 986–993.
- 18 S.-N. Li, Z.-R. Yu, B.-F. Guo, K.-Y. Guo, Y. Li, L.-X. Gong, L. Zhao, J. Bae and L.-C. Tang, *Nano Energy*, 2021, **90**, 106502.
- 19 M. Wu, M. He, Q. Hu, Q. Wu, G. Sun, L. Xie, Z. Zhang, Z. Zhu and A. Zhou, *ACS Sens.*, 2019, **4**, 2763–2770.
- 20 L. Jin, C. Wu, K. Wei, L. He, H. Gao, H. Zhang, K. Zhang, A. M. Asiri, K. A. Alamry and L. Yang, *ACS Appl. Nano Mater.*, 2020, **3**, 12071–12079.
- 21 J. Wang, Y. Yang and Y. Xia, *Sens. Actuators, B*, 2022, **353**, 131087.
- 22 L. Zhao, Y. Zheng, K. Wang, C. Lv, W. Wei, L. Wang and W. Han, *Adv. Mater. Technol.*, 2020, **5**, 1–8.
- 23 C. Yu, J. He and J. Lu, *Small*, 2022, 2204023.
- 24 C. Yu, H.-Z. Lin, J. Zhou, X.-F. Cheng, J.-H. He, H. Li, Q.-F. Xu, N.-J. Li, D.-Y. Chen and J.-M. Lu, *J. Mater. Chem. A*, 2020, **8**, 1052–1058.
- 25 Z. Wang, L. Huang, X. Zhu, X. Zhou and L. Chi, *Adv. Mater.*, 2017, **29**, 1703192.
- 26 M. Boota, M. Pasini, F. Galeotti, W. Porzio, M. Q. Zhao, J. Halim and Y. Gogotsi, *Chem. Mater.*, 2017, **29**, 2731–2738.
- 27 J. Zhou, S. H. Hosseini Shokouh, H. Komsa, L. Rieppo, L. Cui, Z. Lv and K. Kordas, *Adv. Mater. Technol.*, 2022, 2101565.
- 28 X. Li, J. Xu, Y. Jiang, Z. He, B. Liu, H. Xie, H. Li, Z. Li, Y. Wang and H. Tai, *Sens. Actuators, B*, 2020, 128144.
- 29 D. E. Lynch and D. G. Hamilton, *Eur. J. Org. Chem.*, 2017, 3897–3911.
- 30 R. R. Avirah, K. Jyothish and D. Ramaiah, *J. Org. Chem.*, 2008, **73**, 274–279.
- 31 H. Wang, Y. Wu, Y. Zhang, M. Zhou, S. Xu and Z. Li, *Optik*, 2021, 167325.
- 32 M. C. Pham, M. Oulahyane, M. Mostefai and P. C. Lacaze, *Synth. Met.*, 1997, **84**, 411–412.
- 33 A. Sarycheva and Y. Gogotsi, *Chem. Mater.*, 2020, **32**, 3480–3488.
- 34 M. Boota, M. Pasini, F. Galeotti, W. Porzio, M.-Q. Zhao, J. Halim and Y. Gogotsi, *Chem. Mater.*, 2017, **29**, 2731–2738.
- 35 L. Verger, C. Xu, V. Natsu, H.-M. Cheng, W. Ren and M. W. Barsoum, *Curr. Opin. Solid State Mater. Sci.*, 2019, **23**, 149–163.
- 36 S. Rani, M. C. Bhatnagar, S. C. Roy, N. K. Puri and D. Kanjilal, *Sens. Actuators, B*, 2008, **135**, 35–39.
- 37 S. J. Kim, H.-J. Koh, C. E. Ren, O. Kwon, K. Maleski, S.-Y. Cho, B. Anasori, C.-K. Kim, Y.-K. Choi and J. Kim, *ACS Nano*, 2018, **12**, 986–993.
- 38 S. Feng, F. Farha, Q. Li, Y. Wan, Y. Xu, T. Zhang and H. Ning, *Sensors*, 2019, **19**, 3760.
- 39 Z. Liu, D. Han, L. Liu, D. Li, X. Han, Y. Chen, X. Liu, K. Zhuo, Y. Cheng and S. Sang, *Sens. Actuators, B*, 2023, **378**, 133149.
- 40 J. Zhou, M. Bagheri, T. Järvinen, C. Pravda Bartus, A. Kukovecz, H.-P. Komsa and K. Kordas, *ACS Appl. Mater. Interfaces*, 2021, **13**, 59067.
- 41 A. H. Assen, O. Yassine, O. Shekhah, M. Eddaoudi and K. N. Salama, *ACS Sens.*, 2017, **2**, 1294–1301.
- 42 W. Y. Chen, S. N. Lai, C. C. Yen, X. Jiang, D. Peroulis and L. A. Stanciu, *ACS Nano*, 2020, **14**, 11490–11501.
- 43 Y. Guo, M. Zhong, Z. Fang, P. Wan and G. Yu, *Nano Lett.*, 2019, **19**, 1143–1150.
- 44 É. Bozó, H. Ervasti, N. Halonen, S. H. H. Shokouh, J. Tolvanen, O. Pitkanen, T. Jarvinen, P. S. Palvolgyi, A. Szamosvolgyi and A. Sápi, *ACS Appl. Mater. Interfaces*, 2021, **13**, 49301–49312.
- 45 N. Kurra, B. Ahmed, Y. Gogotsi and H. N. Alshareef, *Adv. Energy Mater.*, 2016, **6**, 1601372.
- 46 A. Bhaskar, Y.-W. Yang, Z.-R. Yang, F.-H. Lin and C.-J. Liu, *Ceram. Int.*, 2015, **41**, 7989–7995.
- 47 Q. W. Li, Y. Li, X. F. Zhang, S. B. Chikkannanavar, Y. H. Zhao, A. M. Dangelewicz, L. X. Zheng, S. K. Doorn, Q. X. Jia and D. E. Peterson, *Adv. Mater.*, 2007, **19**, 3358–3363.
- 48 J. L. Hart, K. Hantanasirisakul, A. C. Lang, B. Anasori, D. Pinto, Y. Pivak, J. T. van Omme, S. J. May, Y. Gogotsi and M. L. Taheri, *Nat. Commun.*, 2019, **10**, 1–10.
- 49 P. Khakbaz, M. Moshayedi, S. Hajian, M. Soleimani, B. B. Narakathu, B. J. Bazuin, M. Pourfath and M. Z. Atashbar, *J. Phys. Chem. C*, 2019, **123**, 29794–29803.
- 50 M. Alhabeab, K. Maleski, B. Anasori, P. Lelyukh, L. Clark, S. Sin and Y. Gogotsi, *Chem. Mater.*, 2017, **29**, 7633–7644.
- 51 A. Tkatchenko and M. Scheffler, *Phys. Rev. Lett.*, 2009, **102**, 73005.

